Structured Iterative Alternating Sparse Matrix Decomposition for Thermal Imaging Diagnostic System

Li Liu[1], Bin Gao[1*], Shichun Wu[1], Junaid Ahmed[1], Wai Lok Woo[2], Jianwen Li[3], Yongjie Yu[3]

[1]School of Automation, University of Electronic Science and Technology of China, China

[2]Faculty of Engineering and Environment, Northumbria University, England, UK

[3] Chengdu aircraft industry Co., Ltd.

*Corresponding author: bin_gao@uestc.edu.cn

Abstract: In this paper, we propose a structured iterative alternating sparse matrix decomposition to efficiently decompose the input multidimensional data from active thermography into the sum of a low-rank matrix, a sparse matrix, and a noise matrix. In particular, the sparse matrix is further factorized into a pattern constructed dictionary matrix and a coefficient matrix. The estimation of the dictionary matrix and coefficient matrix is based on integrating the vertex component analysis with the framework of the alternating direction method of multipliers. In addition, the joint structure sparsity and nonnegative constraint are emphasized as part of the learning strategy. In order to verify the effectiveness and robustness of the proposed method, experimental studies have been carried out by applying the proposed method to thermal imaging diagnostic system for carbon fiber reinforced plastics(CFRP) defects detections. The validation study has been conducted by comparing the proposed method with the current state-of-the-art algorithms. The results indicate that the proposed method significantly improves the contrast ratio between the defective regions and the non-defective regions.

Keywords: sparse decomposition, low-rank estimation, thermography defect detection

1. Introduction

Composite materials have been widely used in many fields such as aerospace, high-speed rail, automotive, etc. With the wide application of composite materials in various fields, the demand for composite material safety testing is increasing. Therefore, non-destructive testing(NDT) technology is particularly important for the safety assessment of composite materials [1]. Several traditional NDT techniques such as penetrant testing, eddy current testing, ultrasonic testing, and infrared thermography have been conducted in defect detection of composite materials [2]. Optical pulsed thermography(OPT) is a vision based NDT technology developed based on infrared temperature measurement and optical imaging [3]. Since OPT has the advantages of non-contact, non-invasive and fast, it has become the key technology to guarantee the quality of composite material. There are some strategies that focus on the excitation signal for defect detection capability enhancement, Busse *et al*. [4] proposed lock-in

thermography for NDT evaluation of materials. Mulaveesala *et al.* [5] proposed a pulse-compression approach to infrared NDT characterization and frequency-modulated thermal wave imaging to detect sub-surface defects [6]. Silipigni *et al*. [7] proposed an optimized pulse-compression technique for infrared thermography NDT evaluation. Laureti *et al*. [8] conducted a comparative study between linear and non-linear frequency-modulated pulse-compression thermography. Wu *et al.* [9] proposed halogen optical referred pulse-compression thermography for defect detection of CFRP.

Theoretically, defects can be directly observed from the original image collected by the OPT system, however, due to the influence of noise, feature extraction algorithms are required to enhance the defect detection. Maldague *et al*. [10,11] proposed a pulse phase thermography (PPT) technique based on Fourier transform to extract the frequency domain characteristics of the thermal data. Shepard *et al*. [12] proposed a thermal signal reconstruction (TSR) method for enhancing the visibility of the thermography sequence by fitting the log-time temperature evolution. Zauner *et al*. [13] proposed pulsed phased thermography with the wavelet transform which preserves the time information of the signal since PPT loses the temporal information.

In addition, researchers have applied matrix factorization techniques for defect feature extraction. Principal component analysis (PCA) has been widely used in thermal imaging systems [14]. It is used to calculate the principal components of the temporal data for enhancing the thermal contrast of defect information. Rajic *et al*. [15] proposed a principal component thermography (PCT) algorithm to enhance flaw contrast and characterize flaw depth in composite structures. Some improved algorithms based on PCA have been proposed as well. Yousefi *et al*. [16] proposed candid covariance-free incremental principal component thermography for thermal NDT testing and applied the K-medoids clustering approach to segment the defects in the specimens. Low-rank sparse principal component thermography [17,18] has been proposed by applying both L_1 and L_2 norm to test CFRP, Bell Tower, and wall infrared sets. A comparative study of PCA and partial least squares thermography on NDT investigation of paintings on canvas is proposed in [19]. In addition, Yang *et al*. [20] proposed independent component analysis (ICA) to improve the thermal contrast for CFRP debond detection. Lu *et al*. [21] proposed an ensemble variational Bayes tensor factorization (EVBTF) to conduct the super-resolution of the debond detection by deep mining the sparse tensor. It is based on the variational Bayesian framework [22] which decomposes the given tensor into a low-rank tensor, a sparse tensor, and a noise tensor. The decomposition procedure is performed multiple times on the low-rank matrix until the sparse matrix satisfies the requirement of defect detection. Ahmed *et al.* [23] proposed a sparse low-rank matrix factorization (S-MoG) algorithm for debond detection in CFRP composite based on integrating the mixture of Gaussian (MoG) model and multilayer structure [24].

Matrix factorizations are widely used in many industrial applications. The matrix factorization problem can be solved by a set of traditional factorization methods such as SVD [25]. With the

development in various fields, a family of matrix factorization models has been proposed such as non-negative matrix factorization (NMF), sparse representation, robust principal component analysis (RPCA), etc.

NMF [26] solves the problem of $\mathbf{V} = \mathbf{WH}$ where $\mathbf{V}$ is a given non-negative matrix, $\mathbf{W}$ and $\mathbf{H}$ are unknown with non-negative constraint. It is noted that in practical applications, the solution of sparse decomposition has attracted considerable attention [27]. In recent years, NMF has been applied in action detection [28], recommender systems [29], link prediction in temporal networks [30], etc. The research of NMF on thermal imaging are mentioned in [31,32,33]. The sparse representation model utilizes the training samples to learn a complete dictionary to obtain the sparse representation of the signal. In addition, sparse representation has been widely used in image processing, such as image fusion [34], classification [35], object detection [36], etc. In particular, Wright *et al.* [37,38] defined the problem of decomposing a given data matrix into the sum of a low-rank matrix and a sparse matrix as RPCA which can be described to solve $\mathbf{Y}=\mathbf{L}+\mathbf{S}$ with unknown $\mathbf{L}$ (low-rank matrix) and $\mathbf{S}$ (sparse matrix). This problem can be represented by the following convex optimization problem;

$$\min_{\mathbf{L},\mathbf{S}} \|\mathbf{L}\|_* + \|\mathbf{S}\|_1 \quad \text{s.t.} \quad \mathbf{L}+\mathbf{S}=\mathbf{Y} \tag{2}$$

where $\|\cdot\|_*$ denotes nuclear norm, $\|\cdot\|_1$ denotes the L_1 norm. The optimization problem (1) is termed as the robust principal component pursuit (RPCP). In the real situation, $\mathbf{Y}$ contains noise, that is, $\mathbf{Y}=\mathbf{L}+\mathbf{S}+\mathbf{N}$, then (1) becomes

$$\min_{\mathbf{L},\mathbf{S}} \|\mathbf{L}\|_* + \|\mathbf{S}\|_1 \quad \text{s.t.} \quad \|\mathbf{L}+\mathbf{S}-\mathbf{Y}\|_F^2 < \delta \tag{2}$$

where $\|\cdot\|_F$ denotes the Frobenius norm. The optimization problem (2) is termed as the stable principal component pursuit (SPCP). The RPCA has been used in applications such as target tracking [39] and hyperspectral image processing [40].

Although the existing feature extraction algorithms can enhance defects detections, they have limited or poor performance for detecting weak defects (weak thermal signatures from hard-detectable defects) on complex and irregular surfaces. To deal with these limitations, we propose a structured iterative alternating sparse matrix decomposition model to extract structured sparse features of thermal imaging data for debond detection. The model decomposes the given matrix into a low-rank component, a sparse component and a noise component. The model can efficiently enhance the contrast ratio between the defective and non-defective regions significantly. In addition, only a few requirements are needed for parameter setting and this is validated by carrying out robustness test on different samples. Six different CFRP samples with various sizes of debond defects at different depth levels are used to test the robustness and efficiency of the proposed algorithm. Comparison studies have been undertaken with RPCA-based algorithms and state-of-the-art thermography algorithms. In addition, the results were quantitatively validated by using event-based F-Score [41] and signal-to-noise ratio(SNR) [42].

The remaining of the paper has been organized as follows: The details of the proposed method and the quantitative detectability assessment indicators are described in Section 2. The experiment and result analysis are carried out in Section 3. Conclusion and further work are outlined in Section 4.

2. Methodology

2.1. Proposed Model

In the proposed model, we decompose the given matrix into three matrices, which is $\mathbf{Y} = \mathbf{L} + \mathbf{S} + \mathbf{N}$, where **Y** represents the original data extracted from the infrared (IR) camera, **L** represents the low-rank matrix, **S** represents the sparse matrix and **N** represents the noise matrix. In general, defects are spatially sparse, that is, the sparse matrix **S** contains the structure information of defects. Different defects have different spatial-temporal thermal pattern since this is attributed to the fact that the size and depth of the defects are different. We introduce dictionary matrix **D** to represent the structured thermal pattern. Thus, the sparse matrix **S** can be factorized into **a** dictionary matrix **D** and a coefficient matrix **W**. The model thus becomes $\mathbf{Y} = \mathbf{L} + \mathbf{DW} + \mathbf{N}$. In particular, Fig. 1 illustrates the strategy framework of the proposed method.

a. Background modelling

For weak signal extraction problem such as defect detection, most of the observed signals are background traces, only a small amount of defect information exists in the thermographic sequence and they are unavoidably covered by the background traces. The proposed method adopts a strategy of removing the strong interference signal and simultaneously enhancing the contrast for defect signal from the remaining signal by estimating the background, and then subtracting the background data (**L**) from the observed data (**Y**) to enhance a rough positioning of the defect data (**S**).

b. Mining sparse structure

The estimation of the background paves the way forward for extracting the defect signal. It requires a dictionary matrix to characterize and subsequently enhance the thermal pattern of the defects. The expected enhancement by the dictionary matrix will ensure that the estimated defect signal does not only deviate from the original physical properties but also separate it from other components. In theory, defects and background will show completely different features, however, due to the effects of lateral and longitudinal thermal diffusion, the observed signals are not the expected feature signals as they are superimposed by the expected features. It hypothesizes that the expected features spanning a high-dimensional space, and since the observed data is located in this high dimensional space, we can describe this characteristic with a simplex. In geometry, a simplex is a generalization of the notion of a triangle or tetrahedron to arbitrary dimensions. Specifically, a k-simplex is a k-dimensional polytope which is the convex hull of its k + 1 vertices. Thus, we assume that there is a simplex that wraps the points of $\mathbf{Y} - \mathbf{L}$ which can be seen as a mixture of vertices. These vertices are the thermal patterns, that is, the dictionary

D. Once the vertices are found, the relative weights of the vertices are further updated to obtain the structure of the sparse data. The procedure will be iteratively alternated until convergence.

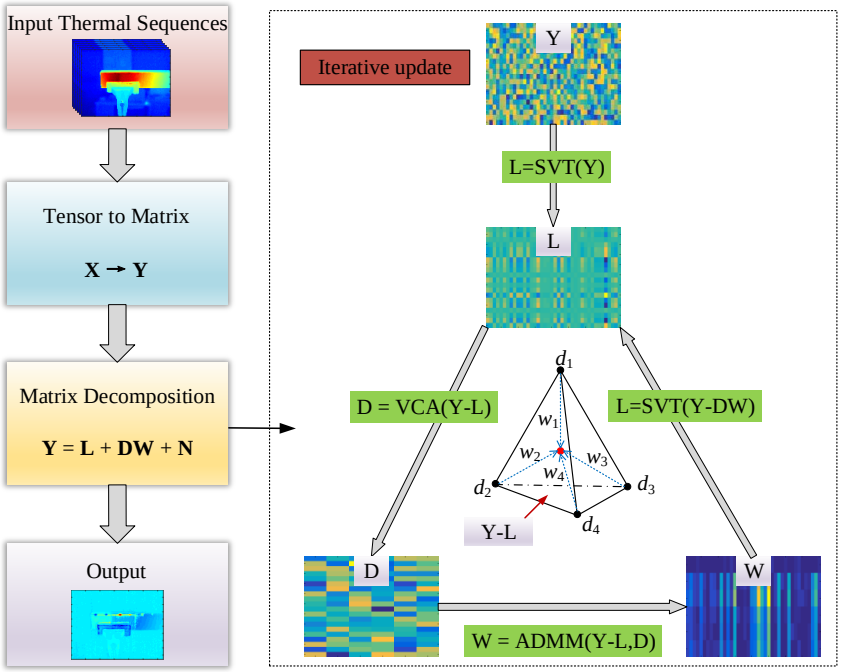

Fig. 1. Framework of the proposed algorithm. The proposed sparse matrix decomposition algorithm decomposes the given matrix into a low-rank component(**L**), a sparse component(**S**) and a noise component(**N**), the sparse component further decomposed into a dictionary matrix(**D**) and a coefficient matrix(**W**). The model estimates each component in an iterative and alternating manner.

2.2. Alternating Structure Sparse Matrix Decomposition

In order to enhance the defect information, the following minimization problem is generated

$$\min_{\mathbf{L},\mathbf{W}} \left\{ \mu \operatorname{rank}(\mathbf{L}) + \lambda \|\mathbf{W}\|_{2,0} + \|\mathbf{Y}-\mathbf{L}-\mathbf{D}\mathbf{W}\|_F^2 \right\} \quad \text{subject to: } \mathbf{W} \geq \mathbf{0} \tag{3}$$

The parameter λ and μ in the formula are the regularization coefficient， the larger the coefficient, the stronger the regularization effect. $\mathbf{W} \geq \mathbf{0}$ is the weight nonnegativity constraint. However, (3) is an NP-hard problem due to rank$(\cdot)$ and$\|\cdot\|_{2,0}$. To simplify the problem, we relax these terms to convex proxies. We use $\|\cdot\|_*$instead of rank$(\cdot)$, and $\|\cdot\|_{2,1}$instead of $\|\cdot\|_{2,0}$. The minimization problem becomes

$$\min_{\mathbf{L},\mathbf{W}} \left\{ \mu \|\mathbf{L}\|_* + \lambda \|\mathbf{W}\|_{2,1} + \|\mathbf{Y}-\mathbf{L}-\mathbf{D}\mathbf{W}\|_F^2 + l_{R+}(\mathbf{W}) \right\} \tag{4}$$

In video processing, it is hypothesized that pixels located in the same region will exhibit similar spatial-temporal characteristics. Thus, both spatial and time-domain features are considered highly correlated. Since the sparse matrix represents the structured thermal pattern, a common sparsity pattern is embedded. In [43], researchers adopted $L_{2,1}$ norm defined by$\|\mathbf{X}\|_{2,1} = \Sigma_{i=1}^{n} \|\mathbf{x}_i\|_2$where $\mathbf{x}_i$ denotes the i-th row of $\mathbf{X}$ to solve the joint sparsity model for pixels in a small neighborhood. In (4), $\|\mathbf{W}\|_{2,1} =$

$\Sigma_{i=1}^{q}\|\mathbf{w}_i\|_2$ denotes the $L_{2,1}$ norm of **W**, $\mathbf{w}_i$ denotes the *i*-th row of **W**, we consider sparsity and correlation of **W** through $L_{2,1}$ norm. The thermal features are stored in the columns of the dictionary matrix. The reason we expect **W** to be sparse is to select the features from the dictionary matrix. As shown in Fig. 2 below, the first row of **W** is 0, indicating that the feature in the first column of **D** has no contribution. We require a certain row of **W** to be 0, which means the sum of the squares of the elements in the row is 0. Thus, we regularize each row with the L_2 norm to obtain a vector and use the L_1 norm to regularize this vector to enable feature selection. Thus, this is termed as the $L_{2,1}$ norm. The second column of **D** in Fig. 2 is the feature of the defect. If the current target point located at the defective region, the feature will have a large weight as shown in the red square in **W**. When we reconstruct the second row of **W** into an image, the pixel value corresponding to the defective region is larger than the non-defective region, to achieve the purpose of enhancing the defect detection.

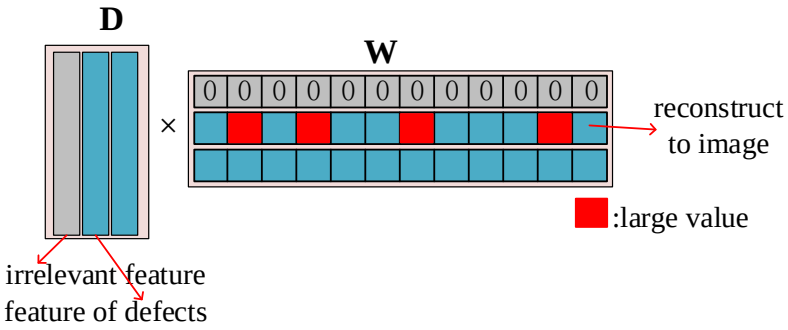

Fig. 2. Sparse matrix(**W**) to select features from the dictionary matrix(**D**).

The last term of (4) is $l_{R+}(\mathbf{W}) = \Sigma_{i=1}^{q} l_{R+}(\mathbf{w}_i)$ and $l_{R+}(\mathbf{w}_i)$has the following form

$$l_{R+}(\mathbf{w}_i) = \begin{cases} 0 & \mathbf{w}_i \geq \mathbf{0} \\ +\infty & otherwise \end{cases} \tag{5}$$

The proposed minimization can be solved iteratively and alternatively in the estimation of **L** in (6), **D** in (7) and **W** in (8). The problem in (6) is convex and can be solved in many ways. As mentioned above, most of the thermal information is the background traces. Singular values often correspond to the dominant information in the matrix since the importance and singular value are positively correlated. Thus the components with larger singular values will be extracted to represent the background, that is, the low-rank matrix. Thus, we employ the Singular Value Thresholding algorithm [44] as a candidate solution. The dictionary matrix **D** in (7) can be estimated by using the vertex component analysis (VCA) [45] as the potential solution. For the problem of (8), we solve it by using the alternating direction method of multipliers (ADMM).

$$\mathbf{L}^{k+1} = \arg\min_{\mathbf{L}} \left\{ \left\| \mathbf{L} - \left(\mathbf{Y} - \mathbf{D}^k \mathbf{W}^k \right) \right\|_F^2 + \mu \|\mathbf{L}\|_* \right\} \tag{6}$$

$$\mathbf{D}^{k+1} \leftarrow \mathrm{VCA}\left(\mathbf{Y} - \mathbf{L}^{k+1} \right) \tag{7}$$

$$\mathbf{W}^{k+1} = \arg\min_{\mathbf{W}} \left\{ \left\| \left(\mathbf{Y} - \mathbf{L}^{k+1} \right) - \mathbf{D}^{k+1}\mathbf{W} \right\|_F^2 + \lambda \|\mathbf{W}\|_{2,1} + l_{R+}(\mathbf{W}) \right\} \tag{8}$$

As mentioned in 2.1, We assume that the sparse data is located in simplex and the defect features are considered as the vertices of the simplex. Taking three-dimensional space as an example, as shown in Fig. 3, $\boldsymbol{d}_1$, $\boldsymbol{d}_2$, $\boldsymbol{d}_3$ and $\boldsymbol{d}_4$ represent thermal features, which is the column of **D**, **S** is a simplex. The idea of VCA is that it finds an initial vertex first, we can choose the pixel with the largest L_2 norm in **Y**. Then it finds the orthogonal projection matrix of the found vertexes in every iteration, the pixel with the largest projection length is the new vertex. Add the new vertex to the vertex set and start the next iteration until all vertexes are found.

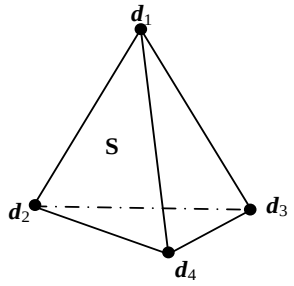

Fig. 3. **S** is a simplex, $\boldsymbol{d}_1$-$\boldsymbol{d}_4$ are vertices.

In the problem (8), since we have already estimated **L** and **D**, we use **Y**' in place of (**Y**-**L**), and consider the following model

$$\mathbf{W}^{k+1} = \arg\min_{\mathbf{W}} \left\{ \left\| \mathbf{Y}' - \mathbf{D}\mathbf{W} \right\|_F^2 + \lambda \left\| \mathbf{W} \right\|_{2,1} + l_{R+}\left(\mathbf{W}\right) \right\} \tag{9}$$

We now apply ADMM to solve this problem [43], the optimization problem (9) can be written as (10).

$$\begin{aligned} &\mathbf{W}^{k+1} = \arg\min_{\mathbf{W}} \left\{ \left\| \mathbf{Y}' - \mathbf{C}_1 \right\|_F^2 + \lambda \left\| \mathbf{C}_2 \right\|_{2,1} + l_{R+}\left(\mathbf{C}_3\right) \right\} \\ &\text{s.t.} \quad \mathbf{C}_1 = \mathbf{D}\mathbf{W} \\ &\qquad \mathbf{C}_2 = \mathbf{W} \\ &\qquad \mathbf{C}_3 = \mathbf{W} \end{aligned} \tag{10}$$

Its augmented Lagrangian function is

$$\begin{aligned} L_\mu\left(\mathbf{W}, \mathbf{C}_1, \mathbf{C}_2, \mathbf{C}_3, \mathbf{U}_1, \mathbf{U}_2, \mathbf{U}_3\right) = &\frac{1}{2}\left\| \mathbf{C}_1 - \mathbf{Y}' \right\|_F^2 + \lambda \left\| \mathbf{C}_2 \right\|_{2,1} + l_{R+}\left(\mathbf{C}_3\right) \\ &+ \frac{\mu}{2}\left\| \mathbf{D}\mathbf{W} - \mathbf{C}_1 - \mathbf{U}_1 \right\|_F^2 + \frac{\mu}{2}\left\| \mathbf{W} - \mathbf{C}_2 - \mathbf{U}_2 \right\|_F^2 + \frac{\mu}{2}\left\| \mathbf{W} - \mathbf{C}_3 - \mathbf{U}_3 \right\|_F^2 \end{aligned} \tag{11}$$

The problem in (11) becomes (12), (13), (14) and (15) as expressed as follows

$$\mathbf{C}_1 = \arg\min_{\mathbf{C}_1} \frac{1}{2}\left\| \mathbf{C}_1 - \mathbf{Y}' \right\|_F^2 + \frac{\mu}{2}\left\| \mathbf{D}\mathbf{W} - \mathbf{C}_1 - \mathbf{U}_1 \right\|_F^2 \tag{12}$$

$$\mathbf{C}_2 = \arg\min_{\mathbf{C}_2} \lambda \left\| \mathbf{C}_2 \right\|_{2,1} + \frac{\mu}{2}\left\| \mathbf{W} - \mathbf{C}_2 - \mathbf{U}_2 \right\|_F^2 \tag{13}$$

$$\mathbf{C}_3 = \arg\min_{\mathbf{C}_3} l_{R+}\left(\mathbf{C}_3\right) + \frac{\mu}{2}\left\| \mathbf{W} - \mathbf{C}_3 - \mathbf{U}_3 \right\|_F^2 \tag{14}$$

$$\mathbf{W} = \arg\min_{\mathbf{W}} \frac{\mu}{2}\left\| \mathbf{D}\mathbf{W} - \mathbf{C}_1 - \mathbf{U}_1 \right\|_F^2 + \frac{\mu}{2}\left\| \mathbf{W} - \mathbf{C}_2 - \mathbf{U}_2 \right\|_F^2 + \frac{\mu}{2}\left\| \mathbf{W} - \mathbf{C}_3 - \mathbf{U}_3 \right\|_F^2 \tag{15}$$

The solution of (12) is expressed as

$$\mathbf{C}_1 = \left(\mathbf{Y}' + \mu\left(\mathbf{DW} - \mathbf{U}_1\right)\right)\left(1+\mu\right)^{-1} \tag{16}$$

The solution of (13) is the vect-soft threshold [46], which is applied to each row of $\mathbf{C}_2$ independently in (17), where r denotes the r-th row of the matrix.

$$\begin{aligned}\mathbf{C}_{2,r} &= \text{vect-soft}\left(\left(\mathbf{W} - \mathbf{U}_2\right)_{\mathrm{r}}, \lambda/\tau\right) \\ &= \left(\mathbf{W} - \mathbf{U}_2\right)_r \frac{\max\left\{\left\|\left(\mathbf{W} - \mathbf{U}_2\right)_r\right\|_2 - \lambda, 0\right\}}{\max\left\{\left\|\left(\mathbf{W} - \mathbf{U}_2\right)_r\right\|_2 - \lambda/\tau, 0\right\} + \lambda/\tau}\end{aligned} \tag{17}$$

The solution of (14) is

$$\mathbf{C}_3 = \max\left(\mathbf{W} - \mathbf{U}_3, 0\right) \tag{18}.$$

The solution of $\mathbf{W}$ can be expressed as follows

$$\mathbf{W} = \left(\mathbf{D}^{\mathrm{T}}\mathbf{D} + 2\mathbf{I}\right)^{-1}\left(\mathbf{D}^{\mathrm{T}}\left(\mathbf{C}_1 + \mathbf{U}_1\right) + \left(\mathbf{C}_2 + \mathbf{U}_2\right) + \left(\mathbf{C}_3 + \mathbf{U}_3\right)\right) \tag{19}.$$

The solution of Lagrange multipliers is (20), (21) and (22).

$$\mathbf{U}_1 = \mathbf{U}_1 - \mathbf{DW} + \mathbf{C}_1 \tag{20}$$

$$\mathbf{U}_2 = \mathbf{U}_2 - \mathbf{W} + \mathbf{C}_2 \tag{21}$$

$$\mathbf{U}_3 = \mathbf{U}_3 - \mathbf{W} + \mathbf{C}_3 \tag{22}$$

The complete description for the proposed algorithm is shown in Table 1.

Table 1. Proposed method

Input: **X** matrix representation of the thermal signal.

Output: thermal low-rank pattern **L**, sparse pattern **S**, coefficient matrix **W**

Pre-processing:

$\mathbf{Y} \leftarrow$ Vectorization (**X**)

Initialize: q (represents the number of columns of **D**), **L**, **D**, **W**

Repeat:

1. $\mathbf{L}^{k+1} \leftarrow \mathrm{SVT}\left(\mathbf{Y} - \mathbf{D}^k\mathbf{W}^k\right)$

2. $\mathbf{D}^{k+1} \leftarrow \mathrm{VCA}\left(\mathbf{Y} - \mathbf{L}^{k+1}\right)$

3. Repeat:

3.1 $\mathbf{C}_1^{i+1} = \left(\left(\mathbf{Y} - \mathbf{L}^{k+1}\right) + \mu\left(\mathbf{D}^{k+1}\mathbf{W}^i - \mathbf{U}_1^i\right)\right)\left(1+\mu\right)^{-1}$

3.2 $\mathbf{C}_{2,r}^{i+1} = \textbf{vect-soft}\left(\left(\mathbf{W}^i - \mathbf{U}_2^i\right)_{\mathbf{r}}, \lambda/\tau\right)$

3.3 $\mathbf{C}_3^{i+1} = \max\left\{\mathbf{W}^i - \mathbf{U}_3^{i+1}, 0\right\}$

3.4 $\mathbf{W}^{i+1} = \left(\left(\mathbf{D}^{k+1}\right)^{\mathrm{T}}\mathbf{D}^{k+1} + 2\mathbf{I}\right)^{-1}\left(\left(\mathbf{D}^{k+1}\right)^{\mathrm{T}}\left(\mathbf{C}_1^{i+1} + \mathbf{U}_1^i\right) + \mathbf{C}_2^{i+1} + \mathbf{U}_2^i + \mathbf{C}_3^{i+1} + \mathbf{U}_3^i\right)$

3.5 $\mathbf{U}_1^{i+1} = \mathbf{U}_1^{i} - \mathbf{D}^{k+1}\mathbf{W}^{i+1} + \mathbf{C}_1^{i+1}$

3.6 $\mathbf{U}_2^{i+1} = \mathbf{U}_2^{i} - \mathbf{W}^{i+1} + \mathbf{C}_2^{i+1}$

3.7 $\mathbf{U}_3^{i+1} = \mathbf{U}_3^{i} - \mathbf{W}^{i+1} + \mathbf{C}_3^{i+1}$

3.8 Update iteration: $i \leftarrow i+1$

Until convergence: $\left\|\mathbf{Y} - \mathbf{L}^{k+1} - \mathbf{D}^{k+1}\mathbf{W}^{i+1}\right\|_2 < \delta$ or reached the maximum number of iterations, return $\mathbf{W}^{k+1}$

4. Update iteration: $k \leftarrow k+1$

Until convergence: $\left\|\mathbf{Y} - \mathbf{L}^{k} - \mathbf{D}^{k}\mathbf{W}^{k}\right\|_2 < \delta$ or reached the maximum number of iterations.

2.3. Quantitative detectability assessment

In order to estimate the detection ability of the proposed algorithm, the event-based F-score and SNR is used to measure the results.

The F-score is defined as follows:

$$F\text{-score} = \left(\beta^2 + 1\right)\frac{Precison \times Recall}{\left(\beta^2 \times Precison\right) + Recall} \tag{23}$$

The precision and recall are defined as follows:

$$Precision = \frac{TP}{TP + FP} \tag{24}$$

$$Recall = \frac{TP}{TP + FN} \tag{25}$$

where TP is true positive, denotes a defect exists and is detected; FP is false positive, denotes no defect exists but is detected; FN is false negative, denotes a defect exists but is not detected; TN is true negative, denotes no defect exists and none is detected. The β in (23) is a default value that determines the weight of the precision and recall. If the value of β is set to 1, it means that the recall is as important as the precision. However, in the field of NDT, it is highly demand to increase the recall rate while ensuring the precision. Therefore, the value of β is set to 2 which means that the recall is more important than the precision.

Fig. 4 shows the interpretation of event-based F-Score. In Fig. 4(a), the thermographic image is divided into 3×8 square grids. According to the label of the sample, each region as an event could be determined by the attribute (defect or non-defect) for the calculation of the F-score. Fig. 4(b) is the label of Fig. 4(a), where 1 indicates that the current grid contains defects, and 0 otherwise. Take Fig. 4(a) as an example, there are 8 events with defect in the figure, the rest are non-defect. According to the above

description, TP is 8, FP is 0, FN is 0, therefore, F-score is 1.

The SNR is used to further evaluate the thermal contrast ratio between the defective and non-defective regions is calculated according to equation (26), where T_d is the temperature of all pixels in the local thermal image 1-1 in Fig. 5, T_{non} is the temperature of all pixels in the local thermal image 1-2 within valid heating area near the defect. The SNR of the entire thermal image is the average of the SNR calculated for all defects.

$$SNR = 20 \times \log 10\left(\frac{T_d}{T_{non}}\right) \tag{26}$$

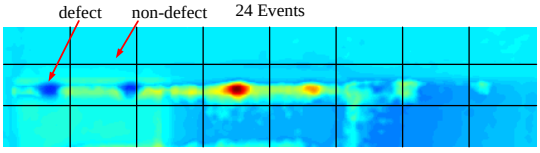

0	0	0	0	0	0	0	0
1	1	1	1	1	1	1	1
0	0	0	0	0	0	0	0

(a) (b)

Fig. 4. Illustration of event based F-Score. (a) Meshing. (b) Corresponding label.

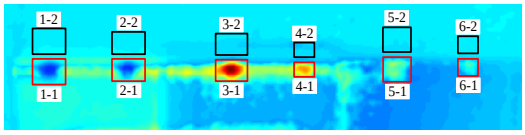

Fig. 5. Illustration of SNR

3. Experiment and result analysis

3.1. Toy examples of the proposed method

In order to verify the proposed method, a toy example is generated shown in Fig. 6. Fig. 6(a) is a real coding of the simulated mixed data, **L** is a rank-one low-rank matrix, **D** is a dictionary matrix with 5 columns, the different 5 curves are shown in Fig. 6(a) which represent 5 dictionaries, **W** is a sparse coefficient matrix, **Y** is the mixed matrix. In addition to the low-rank and the sparse matrix, we added uniform noise in the observation. Parameter setting of the proposed method only requires to set the number of columns in the dictionary matrix **D**, which is represented by q. The set of q is 5.

Fig. 6(b) shows the decomposition results when q is 5. The curves are not as smooth as the real **D** in the estimated dictionary whereas the shape and trend of the curves are consistent. The model has converged when the number of iterations is 15. Fig. 6(c) shows the decomposition result when q is 10. The five colored solid lines in estimated **D** are 1-5 columns of the estimated dictionary matrix. These five curves are similar to the results when q is 5. The five black dashed lines are the 5 overestimated dictionaries, corresponding to the 6-10 columns of the estimated dictionary matrix. The relationship between color and value can be generated from the color bar in **W** since the more the color tends to be blue, the smaller the value. As can be seen from the estimated **W**, the weights of these 5 overestimated

dictionaries are mostly 0, which means, these dictionaries contribute little to the final results. Therefore, they have rare effect on the reconstruction error. The model has not converged when the number of iterations is 15. Table 2 shows the results of 10 experiments for q equal to 5 and 10. From the table, it can be seen that when q is overestimated, the reconstruction error increases. Fig. 6(d) shows the decomposition result when q is 3. Although the reconstruction error converged to a small value, the shape and trend of the three curves in the estimated D are different from the real D in which indicates that the result of decomposition is wrong when q is smaller than the real situation.

In summary, when q is equal to the real situation, the proposed method can effectively estimate the sparse pattern. When q is overestimated, the convergence speed will become slow and the reconstruction error will increase where the weights of the five overestimated dictionaries are mostly 0.

Table 2. The results of q equal to 5 and 10

q	1	2	3	4	5	6	7	8	9	10	Average
5	0.37	0.37	0.38	0.36	0.37	0.37	0.38	0.34	0.37	0.40	0.37
10	0.38	0.39	0.41	0.38	0.38	0.42	0.43	0.36	0.39	0.42	0.40

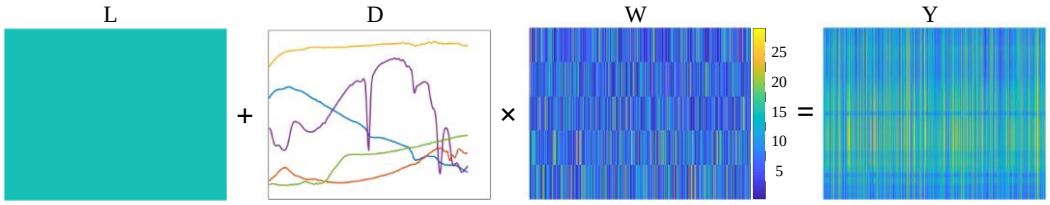

(a)

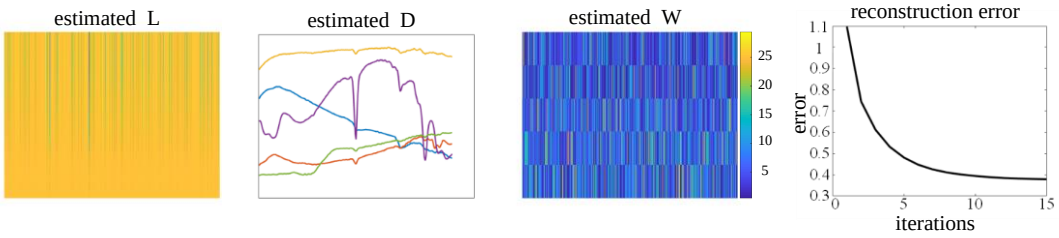

(b)

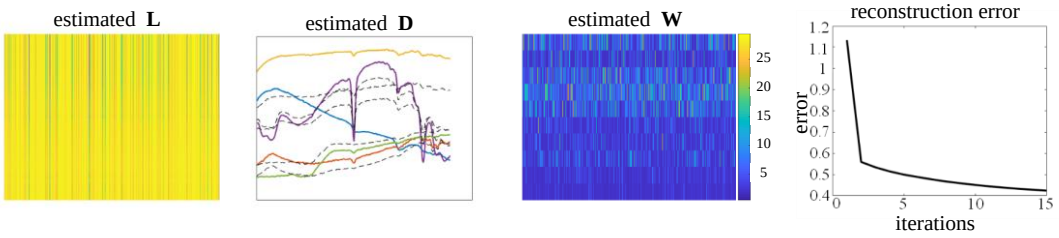

(c)

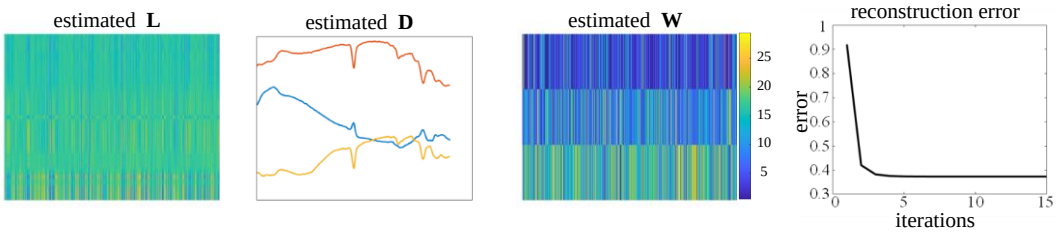

(d)

Fig. 6. Toy examples of the proposed method. (a) Real coding of the simulated mixed data. **L** is the low-rank matrix, **D** is the dictionary matrix, **W** is the coefficient matrix, **Y** is the mixed matrix. (b) Estimated results based on q = 5. (c) Estimated results based on q = 10. (d) Estimated results based on q = 3.

3.2. Experimental setup and Sample Preparation

The Optical Pulse Thermography (OPT) system is shown in Fig. 7. In our experiments, the halogen lamp is used as an excitation and it is controlled by the excitation source. We use IR camera (A655sc) to collect thermal image sequences. It is equipped with an uncooled Vanadium Oxide (VoX) microbolometer detector which can produce 480×640 thermal images. 50Hz frame rate is used to capture the thermal images. The test sample is held by the bracket and placed directly opposite the IR camera and halogen lamp.

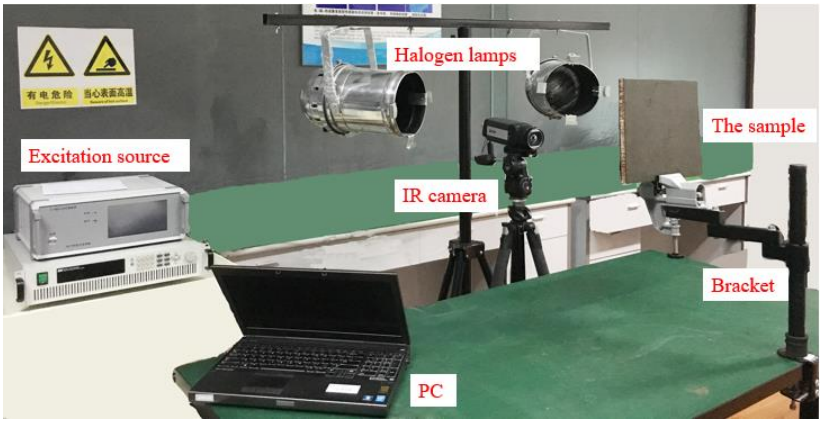

Fig. 7. Optical Pulse Thermography (OPT) system

Six different samples are tested. Four of them are carbon fiber reinforced plastic sample with flat shape, two of them are carbon fiber reinforced plastic sample with curved shape which are more challenging. For the first four samples, they have sub-surface debond defects with different diameters and depths. The latter two samples have debond defects located in the elbow location which are difficult to be detected. The detailed information of these samples can be found in Table 3. Nine sets of experimental data were performed based on these six samples. Due to the honeycomb of test specimen 1, only one-sided defects can be heated in each experiment, the results of specimen 1 correspond to data 1 and data 3.

Table 3. Samples

Number	Specimen	*Picture*
1	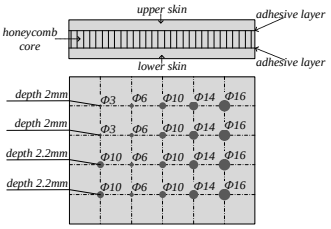	
2	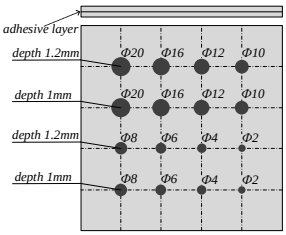	
3	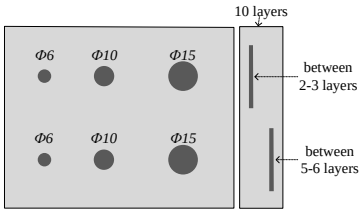	
4	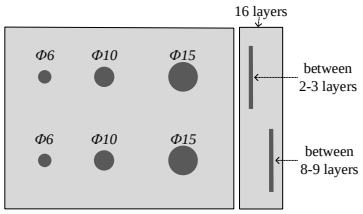	
5	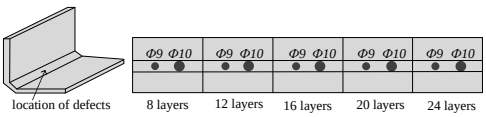	
6	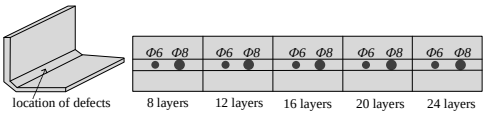	

3.3. Thermographic image description

Let $\mathbf{X} \in \mathbb{R}^{M \times N \times F}$ denotes a tensor containing the thermographic sequence image, $M \times N$, denotes the size of a single thermographic image, F, denotes the length of the sequence or the number of the

frames. Fig. 8(a) shows the selected image from the original thermal sequences and being partitioned in 4 characteristic regions. These 4 regions include the defect region (number 1), the near defect region (number 4, on the test sample with strong interference background), the far defect region (number 3, on the test sample with weak interference background), and the non-thermal background region (number 2, excluding test sample). Fig. 8(b) shows the temperature transient characteristics of the 4 regions (temperature changes with heating and cooling time). It can be seen that region 2 and region 3 are easily distinguished from region 1 whereas the characteristics of region 4 and region 1 are more difficult to be separated.

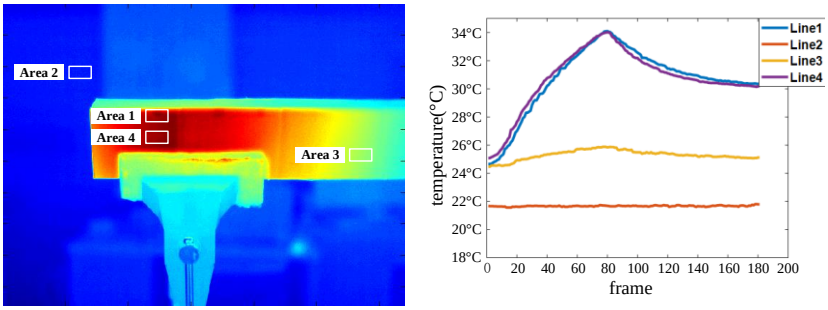

(a) (b)

Fig. 8. Temperature characteristics of thermal data. (a) Four characteristic areas on the thermal image, where area 1 is the defect area; area 2 is the background without specimen area; area 3 is the non-defective area away from defect; area 4 is the non-defective area near defect. (b) Line 1 - line 4 are the temperature transient characteristics corresponding to area 1 - area 4 where line 1 and line 4 are almost identical.

We transform the thermographic sequence data into a matrix $\mathbf{Y} \in \mathbb{R}^{F \times P}$ before decomposing, F denotes the number of frames, the size of P is $M \times N$. As illustrated in Fig. 9, the vec-operator applied on a matrix $\mathbf{X}(:,:,f)$ stacks its columns into a row vector $\text{vec}[\mathbf{X}(:,:,f)]^{\mathrm{T}}$.

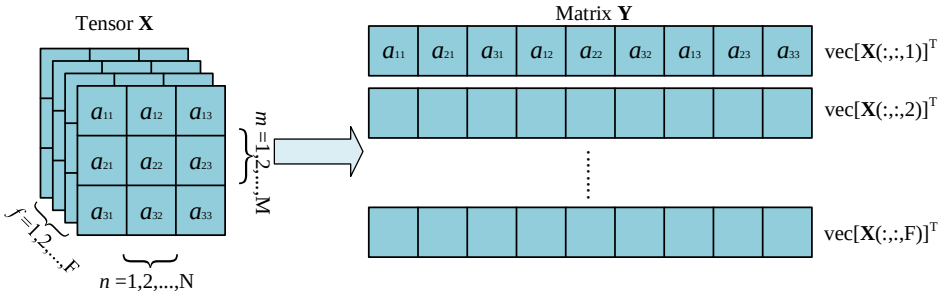

Fig. 9. Illustration of converting a 3-dimensional tensor into a 2-dimensional matrix by vectorising each frame.

3.4. Model analysis

According to the description of 3.3, the defect region and the near defect region is hard to be

separated. The proposed model's strategy is to remove the strong interference signal (background) and simultaneously enhance the contrast for defect signal from the remaining signal. However, there exists only rare defect information in the entire sequence. In other words, most of the thermal image sequence is background traces. The singular value decomposition is selected to approximate the physics behavior of the thermal spatial-transient characteristic. Singular values often correspond to the dominant information in the matrix since the importance and singular value is positively correlated. Thus the components with larger singular values will be extracted to represent the background, that is, the low-rank matrix. With the simple calculation, the singular value decomposition will be able to extract the background signal which is beneficial for subsequent defect information enhancement.

The estimation of the background paves the way forward for the proposed algorithm to extracting the defect signal. It requires a dictionary matrix to characterize and enhance the thermal pattern of the defects. The expected enhancement procedure by the dictionary matrix will ensure that the estimated defect signal does not deviate from the original physical properties but also separate it from other components. The VCA holds high potential to solving the problem. We will prove this choice from two aspects, one is the mathematical connection between thermal physics and VCA, the other is validation by the results.

Due to the effects of lateral and longitudinal thermal diffusion, the observed signals are not the expected feature signals as they are superimposed by the expected features. In Fig. 10(a), we take 4 points *a*, *b*, *c*, and *d*, where point *a* represents the center of defect 2, we assume that the thermal feature of point *a* is the expected feature of defect, point *b* is the edge of defect 2, point *c* is the background near defect 2, point *d* is the background far from defect 2. In Fig. 10(b), line 1-4 correspond to the thermal features of points *a*-*d*. It can be seen that line 1 and line 3 are easy to be distinguished, while line 2 and line 3 are similar. In theory, line 2 is similar to line 1, and line 3 is similar to line 4. However, since point *b* and point *c* are located at the boundary between the defect and the background region, they are affected by thermal diffusion, and the features of the two points can be regarded as the superposition of background and defect features. Thus, it is resulting in the features of point *b* and point *c* are quite similar. From the longitudinal direction, point *a* corresponds to line 1, point *e* corresponds to line 5, the non-defective area above point *e* is more thick than that above point *a*, and the temperature at point *e* is lower than the temperature at point *a*. This shows that the feature of the internal defect transport to the surface is a superposition of features of the defect and the non-defective area above the defect. The above description illustrates that the surface temperature signal we collected by the IR camera is a mixed signal, and the process of finding each signal feature is the process of unmixing. As we described in section 2, the observed data is located in this high dimensional space, simplex, data in simplex can be regarded as linear combination of vertexes which are dictionaries.

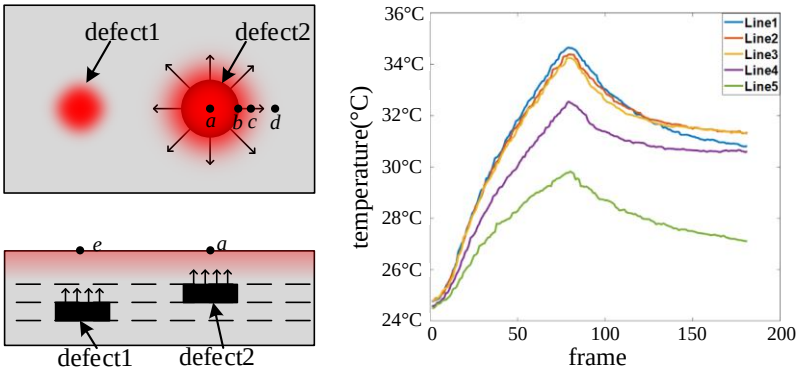

(a) (b)

Fig. 10. (a) Thermal diffusion effect. Point *a*, *b*, and *e* located in defective area, point *c* and *d* located in non-defective area. (b) Line 1-line 5 correspond to the characteristics of the temperature change of points *a*-*e* over time. The temperature characteristics of point *b*(defect) and point *c*(non-defect) are difficult to distinguish. The temperature of point *e*(deeper defect)is lower than point *a*(surface defect).

Fig. 11(a) is a manually selected dictionary, which is the thermal transient sequence of 4 characteristic regions on the image in 3.3. It can be seen that the defect region (line 1) and the non-defect region near the defect region (line 4) are difficult to be distinguished. Fig. 11(b) is the dictionary estimated by VCA. We set the number of columns in the dictionary matrix to 4, and the four lines in the figure represent the four columns of the dictionary matrix, that is, four temperature characteristics. These four estimated characteristic curves are approximately the same in trend as the manually selected features from original thermal sequences, and more importantly, VCA directly enhanced the contrast of lines 1 and line 4. Thus, it satisfies the initial expected enhance procedure where this not only can't deviate from the original physical properties but also separate the defects from the other components.

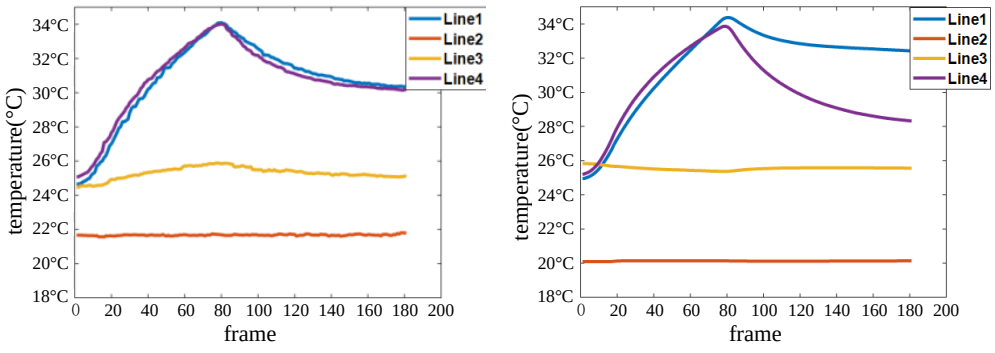

(a) (b)

Fig. 11. Manually selected dictionary vs. VCA estimated dictionary. Line 1 corresponds to the defective area; line 2 corresponds to the background area without test specimen; line 3 corresponds to the non-defective area away from the defect; line 4 corresponds to the non-defective area near the defect. (a) Manually selected dictionary. Line 1 and line 4 are difficult to be distinguished. (b) VCA estimated dictionary. VCA enhanced the contrast between line 1 and line 4

3.5. Result and analysis

In order to evaluate the proposed algorithm, three RPCA based algorithms and five thermal based defect detection algorithms were selected for comparison. The three RPCA algorithms include: SPCP [47], online RPCA(OR-PCA) [48] and EVBTF which solved RPCA problem from the perspective of probability distribution, and proposed for defect detection. The five defect detection algorithms include: PCA, ICA, S-MOG, TSR, PPT. Among them, PCA, ICA, S-MOG are algorithms based on matrix factorization, TSR and PPT are algorithms with physical significance.

SPCP decompose the given matrix into low-rank matrix, sparse matrix and noise matrix, we choose sparse matrix as the result. OR-PCA decompose the given matrix into low-rank matrix and sparse matrix, sparse matrix is corrupted noise that contain few information, therefore, we choose the low-rank matrix as the result. We apply PCA where the first 8 principal components are retained since experiments show that 8 principal components can meet the requirement, and then choose the component which has the best performance. The same setting is conducted for ICA. In TSR, the parameter that needs to be discussed is the order. In the following experiments, we choose the order of 5 to find the best results of TSR. PPT is applied to transfer the time domain signal into the frequency domain. The best phase thermal contrast image is selected for comparison. The parameter setting of the EVBTF and S-MOG is the layer selection, different layers are chosen according to different samples.

The comparison visual results based on these algorithms and the proposed algorithm are given in Figs. 12 and. 13. In addition to the visual results, the results based on computational time are tabulated in Table 4, the comparative quantitative results based on the event-based F-Score (denoted by F_2) and SNR are given in Table 5.

For visual results, we choose a flat sample (sample1) and a curve sample (sample 5) as Fig. 12 and Fig. 13, the remain results can be found in the supplementary file. In these figures, the first row is the results of the three RPCA based algorithms, the second row is the results of three matrix factorization based algorithms, the third row is the results of physical based algorithms and the proposed algorithm.
It can be seen from the results that OR-PCA performs worst among other algorithms since it is an online algorithm and may lost some global temperature characteristics, PPT and TSR have higher defect detection rate on some test samples, but the result images contain a lot of noise compared to other algorithms, the proposed algorithm can extract defects on the thermal images and enhance the defect signals. Compared with other 8 algorithms, the results of the proposed are better and have less noise. From the detection rate, the proposed algorithm can extract more defects and enhance the weak signal of defects. In particular, the detection rate is significantly better than other algorithms, especially for the challenging samples with complex shape. From the aspect of parameter setting, all the detection results of the proposed method are based on the same setting of the parameters in which can validate its

robustness.

Table 4 shows the results based on computational time of algorithms. It can be seen from the results that PCA is the fastest algorithm, the three RPCA based algorithms, and the physical based algorithms are all inefficient. For a task whose detection accuracy requirement is higher than the detection efficiency, the proposed algorithm is acceptable in terms of the computational time

Table 5 shows the F-Score and SNR based results, all the results of F-Score are quoted as a percentage and the average value for all methods is also shown in the table. From the table, it is evident that the proposed algorithm gives the highest F-Score and SNR on average than other algorithms. The 'Inf' in Table 5 denotes positive infinity as there are no background and noise signals around the defects, as can be seen from the corresponding visual results. The calculation of all average SNR removes the results of sample 3 and sample 9, which contain the result of positive infinity. Combining the results of Table 5, the proposed algorithm is better in terms of detection ability and SNR. Even with a few exceptions, such as the F-Score of PCA and ICA in sample 3 is slightly higher than the proposed algorithm, the SNR is much lower than the proposed algorithm.

3.6. Comparison of Different Parameter Settings

In this work, the experimental results show that the proposed method has a high level of performance in defect extraction compared to other conventional detection methods. These results are highly impacted by the selection of the number of columns in the dictionary matrix, we use q to represent it. In the experiments, the number of q is selected as 6. This selection is based on a large number of experiments. In order to illustrate the effect of the value of q, we selected three different samples for validating. Each sample was tested three times by using different levels of q. The visual results of the experiment are shown in Fig. 14. As can be seen from the results in Fig. 14, when the value of q is selected too small (q = 2), a large amount of defect information is flooded by the background. This phenomenon can be seen especially from the third sample as it can hardly detect the defects. When the value of q is selected moderately (q = 6), defects can be detected and the information of detects is significantly enhanced. When the value of q is selected too large (q = 30), the defect can be detected whereas the noise near the defects of the first sample is significantly increased. All defects of the second sample are completely submerged by the noise. In the result of the third sample, not only the vicinity of the defects, the noise of the entire image is significantly increased. From the results of Table 6, when the value of q is set to 6, the values of the F-score and SNR are the highest. In summary, the selection of the number of columns in the dictionary matrix will impact the performance, and set this value to 6 can meet the requirement of the most application.

From the visual perspective, the higher the rank of a matrix, the richer the detailed information it contains. Thus, the rank of the matrix has significant impacts on the detection results. Fig. 14 are the

results of using different rank on two samples. From the results in Fig. 15 (a)-(f) we can see that when the rank of matrix **L** is set to be small, although defects can be detected, the background traces is not well suppressed; when the rank of matrix **L** is set to be moderate, it can enhance defects detections while effectively suppress background traces; when the rank of matrix **L** is set to be large, matrix **L** contains not only background traces but also a large amount of defect's information, resulting in the defect's information in sparse matrix **S** is insufficient, defects are missed and the image contains a lot of noise.

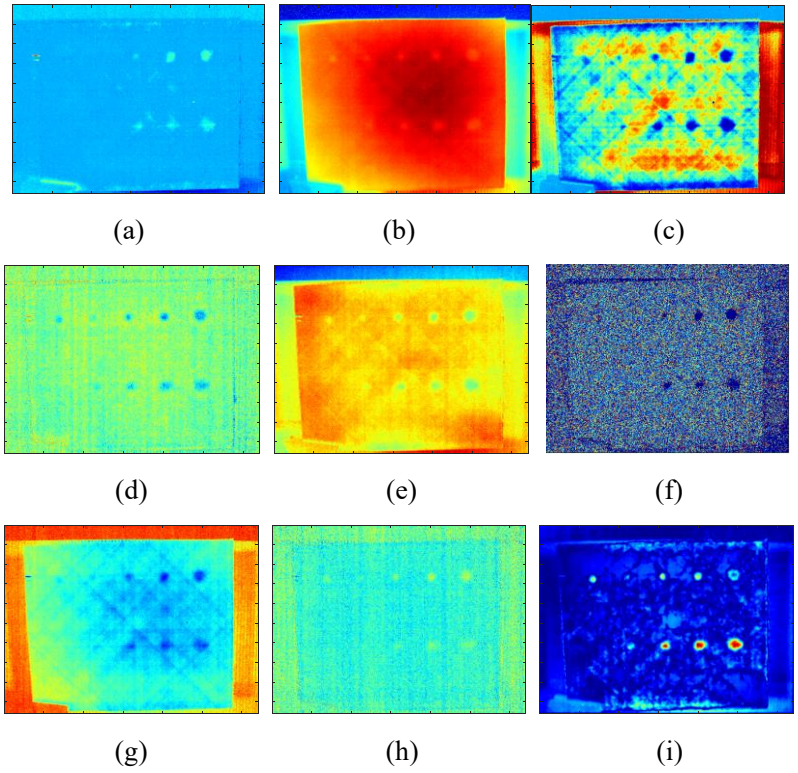

Fig.12. Results of data 1(sample 1). (a)RPCA (b) OR-PCA (c)EVBTF (d)PCA (e)ICA (f)S-MOG (g)PPT (h)TSR (i)Proposed.

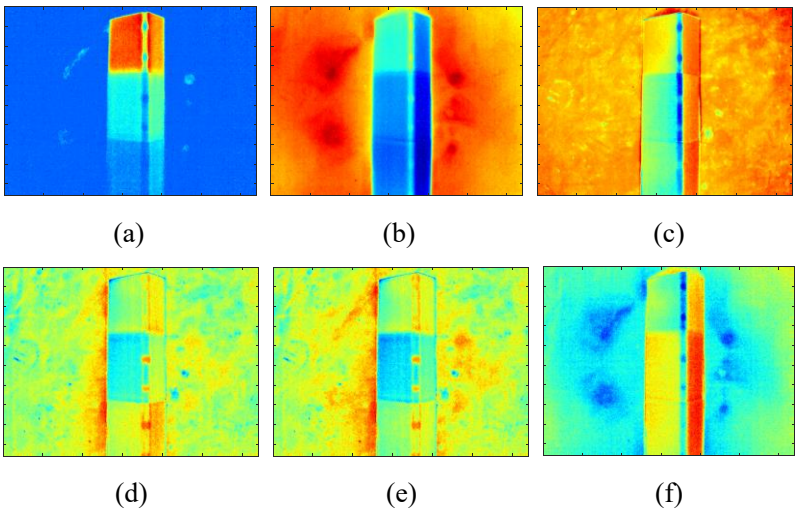

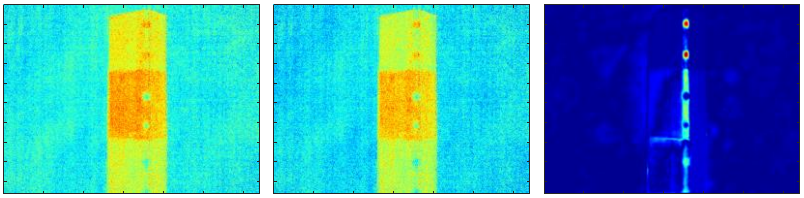

(g) (h) (i)

Fig.13. Results of data 2(sample 5). (a)RPCA (b) OR-PCA (c)EVBTF (d)PCA (e)ICA (f)S-MOG (g)PPT (h)TSR (i)Proposed.

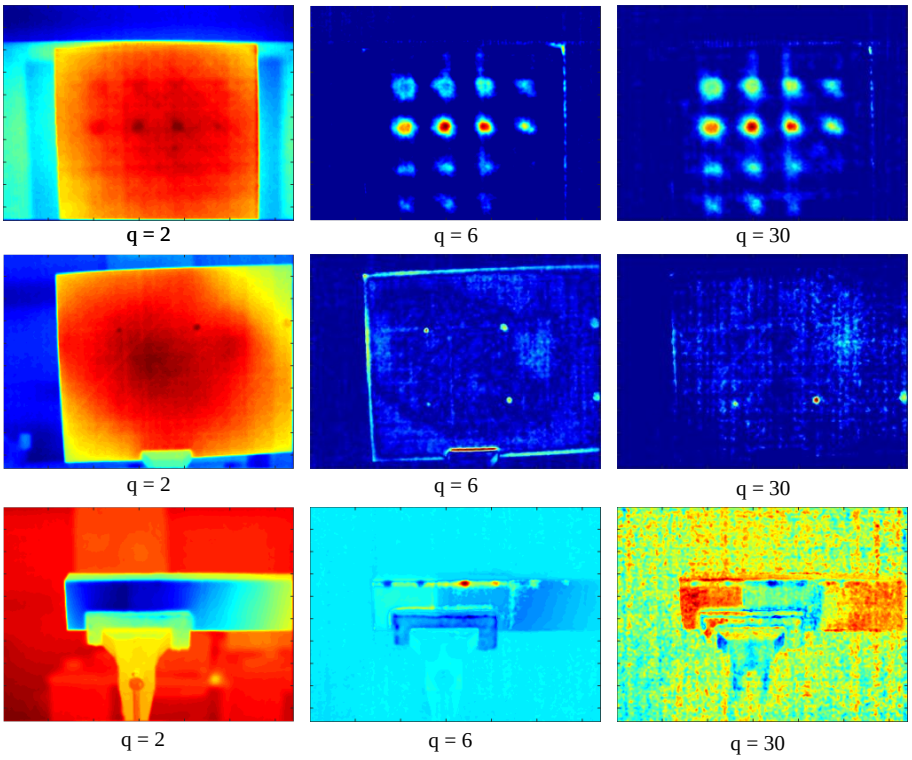

Fig. 14. Visual results for different q.

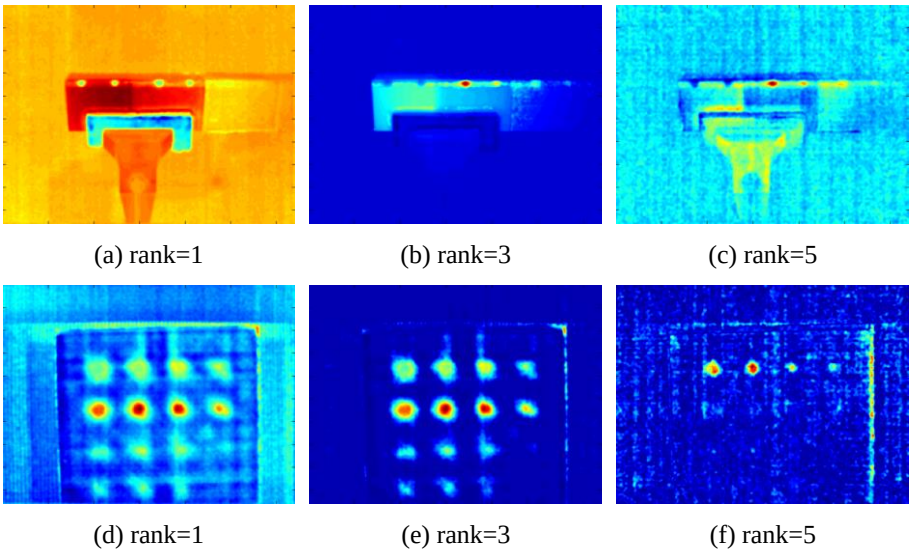

(a) rank=1 (b) rank=3 (c) rank=5

(d) rank=1 (e) rank=3 (f) rank=5

Fig. 15. Detection results for low-rank matrix with different rank. (a) rank is 1, defects are missed, the

image contains lots of background traces. (b) rank is 3, all defects been detected, the background is effectively suppressed. (c) rank is 5, weak defects are covered by noise, and the image contains a lot of noise. (d) rank is 1, defects are missed, the image contains lots of background traces. (e) rank is 3, defects are missed, the background is effectively suppressed and the SNR is enhanced. (f) rank is 5, large number of defects are missed, and the image contains a lot of noise.

Table 4. Performance comparison of computational time

sample	RPCA	OR-PCA	EVBTF	PCA	ICA	S-MOG	TSR	PPT	Proposed
1	342.96	926.14	238.23	1.34	1.61	79.51	118.44	59.04	14.28
2	230.62	785.45	230.12	1.60	1.90	27.34	117.95	59.90	8.32
3	184.23	471.54	239.97	1.02	1.55	29.13	112.47	59.47	7.45
4	194.64	948.67	256.27	1.54	2.06	28.05	125.75	58.13	8.95
5	123.37	327.97	224.02	1.05	1.38	30.3	112.69	57.34	7.00
6	264.15	699.99	361.28	2.24	2.84	44.95	123.19	61.51	12.40
7	280.91	877.26	306.19	1.56	2.03	58.76	118.53	61.15	9.85
8	456.60	587.17	454.35	1.86	2.70	81.65	124.30	62.28	26.51
9	88.82	204.26	182.23	0.90	1.21	15.99	105.28	55.60	6.00
Average	240.70	647.61	276.96	1.46	1.92	43.96	117.62	59.38	11.20

Table 5. Performance comparison of F-score and SNR

sample		RPCA	ORPCA	EVBTF	PCA	ICA	S-MOG	TSR	PPT	Proposed
1	F_2	71.43%	76.47%	86.21%	76.47%	85.23%	71.43%	86.21%	76.47%	92.39%
	SNR	1.88	0.73	17.42	3.49	1.92	11.16	3.68	1.70	18.45
2	F_2	86.53%	84.16%	96.15%	99.06%	90.48%	96.15%	84.16%	96.15%	100%
	SNR	3.54	0.85	7.83	6.62	4.92	9.63	4.24	4.74	17.96
3	F_2	77.52%	53.72%	84.91%	87.36%	87.36%	90.23%	84.62%	86.14%	86.47%
	SNR	7.79	0.92	7.63	9.57	8.51	12.64	5.17	8.31	Inf
4	F_2	84.91%	68.63%	90.91%	90.91%	90.91%	96.15%	92.59%	60%	100%
	SNR	1.64	0.65	4.47	3.59	3.42	4.08	4.51	2.02	22.83
5	F_2	78.95%	0	78.95%	78.95%	78.95%	78.95%	78.95%	78.95%	98.77%
	SNR	7.15	0	4.49	2.63	2.96	9.92	4.99	0.27	6.67
6	F_2	74.47%	74.47%	100%	100%	100%	100%	100%	100%	100%
	SNR	4.11	0.50	1.34	2.96	5.62	9.39	2.02	1.59	30.00
7	F_2	85.23%	94.59%	83.33%	85.71%	94.59%	85.71%	94.59%	97.22%	97.22%

8	SNR	4.7	8.39	8.83	0.33	0.66	13.07	0.70	0.95	29.09
	F_2	88.24%	75.76%	100%	75.76%	97.22%	75.76%	75.76%	100%	100%
9	SNR	4.41	2.35	6.13	2.68	1.40	12.2	9.67	1.64	28.40
	F_2	48.39%	0	62.50%	62.50%	62.50%	48.39%	48.39%	33.33%	69.23%
Average	SNR	11.90	0	4.24	2.67	3.87	6.91	5.13	0.77	Inf
	F_2	77.30%	58.64%	87.00%	84.08%	87.47%	82.53%	82.81%	80.92%	93.79%
	SNR	4.99	1.95	7.22	3.19	2.99	9.92	4.26	1.84	16.99

Table 6. Performance comparison of F-score and SNR

sample		$q = 2$	$q = 6$	$q = 30$
3	F-Score	22.12%	86.47%	84.27%
	SNR	0.87	Inf	29.91
4	F-Score	51.02%	100%	41.67%
	SNR	0.43	22.83	20.91
6	F-Score	0%	98.77%	88.61%
	SNR	0	6.67	3.40

4. Conclusion and Feature Work

In this paper, a structured iterative alternating sparse matrix decomposition has been proposed for thermal imaging diagnostic system. Since different regions on the image have different spatial-temporal thermal characteristics, the physical interpretation of thermal patterns as well as the sparse decomposition has been established. The proposed sparse decomposition method allows abnormal patterns to be extracted automatically for flaw contrast enhancement. The proposed method is able to reduce interference from the background. Compared with current state-of-the-art methods, the evaluation results have shown that the proposed method has the best performance in defect extraction. However, the parameter setting is not fully automated. Future research will focus on defect detection in motion condition, especially for materials containing natural defects.

Acknowledgement

The work was supported by Defense Industrial Technology Development Program (Grant No. JSZL2019205C003), National Natural Science Foundation of China (No. 61971093, No. 61527803, No. 61960206010). The work was supported by Science and Technology Department of Sichuan, China (Grant No.2019YJ0208, Grant No.2018JY0655, Grant No. 2018GZ0047) and Fundamental Research Funds for the Central Universities (Grant No. ZYGX2019J067).

Reference

[1] Abbe S, Degait A, Honorat P, Renon J M. Industrial non destructive testing of composite materials by stimulated infrared thermography[C], Proceedings of the 13th World Conference on Non-Destructive

Testing,1992, 2:703-707.

[2] Zhang, H.*, Yu, L., Hassler, U., Fernandes, H., Genest, M., Robitaille, F., Joncas, S., Holub, W., Sheng, Y. and Maldague, X., (2016). An experimental and analytical study of micro-laser line thermography on micro-sized flaws in stitched carbon fiber reinforced polymer composites. Composites Science and Technology, 126, pp.17-26.

[3] Chulkov A O, Vavilov V P. Hardware and Software for Thermal Nondestructive Testing of Metallic and Composite Materials[C]// 2016:1392–1397.

[4] Wu D, Busse G. Lock-in thermography for nondestructive evaluation of materials[J]. Revue générale de thermique, 1998, 37(8): 693-703.

[5] Mulaveesala R, Vaddi J S, Singh P. Pulse compression approach to infrared nondestructive characterization[J]. Review of Scientific Instruments, 2008, 79(9): 094901.

[6] Mulaveesala R, Tuli S. Implementation of frequency-modulated thermal wave imaging for non-destructive sub-surface defect detection[J]. Insight-Non-Destructive Testing and Condition Monitoring, 2005, 47(4): 206-208.

[7] Silipigni G, Burrascano P, Hutchins D A, et al. Optimization of the pulse-compression technique applied to the infrared thermography nondestructive evaluation[J]. NDT & E International, 2017, 87: 100-110.

[8] Laureti S, Silipigni G, Senni L, et al. Comparative study between linear and non-linear frequency-modulated pulse-compression thermography[J]. Applied optics, 2018, 57(18): D32-D39.

[9] Wu S, Gao B, Yang Y, et al. Halogen optical referred pulse-compression thermography for defect detection of CFRP[J]. Infrared Physics & Technology, 2019, 102: 103006.

[10] X. Maldague, S. Marinetti. Pulse phase infrared thermography[J]. Journal of Applied Physics, 1996,79: 2694–2698.

[11] F. López, V.P. Nicolau, X.B.T.-I.C. on Q.I.T. Maldague. Pulsed Phase Thermography applied on complex structures: modeling and numerical analysis[C]. 11th International Conference on Quantitative Infrared Thermography.

[12] S.M. Shepard, M F Beemer. Advances in thermographic signal reconstruction[J]. SPIE, 2015, 9485: 421–428.

[13] G. Zauner, G. Mayr, G. Hendorfer, C. Wels. Wavelet-based subsurface defect characterization in pulsed phase thermography for non-destructive evaluation[J]. SPIE, 2009, 7248: 1–9.

[14] Ali Sophian, Gui Yun Tian, David Taylor, John Rudlin. A feature extraction technique based on principal component analysis for pulsed Eddy current NDT[J]. NDT & E International, 2003, 36: 37-41.

[15] N. Rajic. Principal component thermography for flaw contrast enhancement and flaw depth characterisation in composite structures[J], Composite Structures, 2002, 58: 521–528.

[16] Yousefi B, Sfarra S, Castanedo C I, et al. Comparative analysis on thermal non-destructive testing

imagery applying Candid Covariance-Free Incremental Principal Component Thermography (CCIPCT)[J]. Infrared Physics & Technology, 2017, 85: 163-169.

[17] Yousefi B, Sfarra S, Sarasini F, et al. Low-rank sparse principal component thermography (sparse-pct): Comparative assessment on detection of subsurface defects[J]. Infrared Physics & Technology, 2019, 98: 278-284.

[18] Sfarra S, Cicone A, Yousefi B, et al. Improving the detection of thermal bridges in buildings via on-site infrared thermography: The potentialities of innovative mathematical tools[J]. Energy and Buildings, 2019, 182: 159-171.

[19] Zhang H, Sfarra S, Saluja K, et al. Non-destructive investigation of paintings on canvas by continuous wave terahertz imaging and flash thermography[J]. Journal of Nondestructive Evaluation, 2017, 36(2): 34.

[20] G. Yang, G.Y. Tian, P.W. Que, T.L. Chen. Independent Component Analysis – Based Feature Extraction Technique for Defect Classification Applied for Pulsed Eddy Current NDE[J]. Research in Nondestructive Evaluation,2009, 9847.

[21] P. Lu, B. Gao, Q. Feng, Y. Yang, W.L. Woo, G.Y. Tian. Ensemble Variational Bayes Tensor Factorization for Super Resolution of CFRP Debond Detectionm[J]. Infrared Physics & Technology, 2017, 85:335–346.

[22] Zhao, Qibin et al. Bayesian Robust Tensor Factorization for Incomplete Multiway Data[J]. IEEE Transactions on Neural Networks and Learning Systems, 2015, 27: 736–48.

[23] J. Ahmed, B. Gao, G.Y. Tian, Y. Yang, Y.C. Fan. Sparse Ensemble Matrix Factorization for Debond Detection in CFRP Composites Using Optical Thermography[J]. Infrared Physics & Technology, 2018, 92: 392-401.

[24] H. Yong, D. Meng, W. Zuo, L. Zhang. Robust Online Matrix Factorization for Dynamic Background Subtraction[J]. IEEE Transactions on Pattern Analysis and Machine Intelligence, 2018,40: 1726–1740.

[25] Rehurik, R. Scalability of Semantic Analysis in Natural Language Processing, Ph.D. thesis, Masaryk University, Brno, Czech Republic, 2011.

[26] Lee, Daniel D, and H Sebastian Seung. Learning the Parts of Objects by Non-Negative Matrix Factorization[J]. Nature,1999, 401: 788–91.

[27] Z. Yang, G. Zhou, S. Xie, S. Ding, J.-M. Yang, J. Zhang. Blind spectral unmixing based on sparse nonnegative matrix factorization[J]. IEEE Trans. Image Process, 2011, 20: 1112–1125.

[28] Adeli-mosabbeb, Ehsan, and Mahmood Fathy. Non-Negative Matrix Completion for Action Detection[J]. Image and Vision Computing, 2015, 39: 38–51.

[29] Bobadilla, Jesús, Rodolfo Bojorque, and Remigio Hurtado. Recommender Systems Clustering Using Bayesian Non Negative Matrix Factorization[J]. IEEE Access, 2017, 6: 3549–64.

[30] X. Ma, P. Sun, G. Qin. Nonnegative matrix factorization algorithms for link prediction in temporal networks using graph communicability[J], Pattern Recognition, 2017, 71: 361–374.

[31] Yousefi B, Sfarra S, Ibarra-Castanedo C, et al. Thermography data fusion and nonnegative matrix factorization for the evaluation of cultural heritage objects and buildings[J]. Journal of Thermal Analysis and Calorimetry, 2019, 136(2): 943-955.

[32] Marinetti S, Finesso L, Marsilio E. Matrix factorization methods: Application to thermal NDT/E[J]. NDT & E International, 2006, 39(8): 611-616.

[33] Yousefi B, Ibarra-Castanedo C, Maldague X P. Application of Sparse Non-Negative Matrix Factorization in infrared non-destructive testing[C]//Proceedings of the 3rd Asian Conference on Quantitative Infrared Thermography, Tokyo, Japan. 2019: 1-5.

[34] Xing, Changda et al. Image Fusion Method Based on Spatially Masked Convolutional Sparse Representation[J]. Image and Vision Computing, 2019, 90: 103806.

[35] Hsu, Pai-hui, and Ying-ying Cheng. Hyperspectral Image Classification via Joint Sparse Representation[C]. IGARSS, 2019, 2997–3000.

[36] Yi, Liu, Zhang Qiang, Han Jungong, and Wang Long. Salient Object Detection Employing Robust Sparse Representation and Local Consistency[J]. Image and Vision Computing,2017, 69: 155–67.

[37] Wright, John et al. Robust Principal Component Analysis: Exact Recovery of Corrupted Low-Rank Matrices via Convex Optimization[C]. In Advances in Neural Information Processing Systems, 2009, 2080–2088.

[38] Candès, Emmanuel J, Xiaodong Li, Yi Ma, and John Wright. Robust Principal Component Analysis?[J]. Journal of the ACM (JACM), 2011, 58:11.

[39] Wan M, Gu G, Qian W, et al. Total variation regularization term-based low-rank and sparse matrix representation model for infrared moving target tracking[J]. Remote Sensing, 2018, 10(4): 510.

[40] Yang Xu et al. Joint Reconstruction and Anomaly Detection from Compressive Hyperspectral Images Using[J]. IEEE Transactions on Geoscience and Remote Sensing, 2018, 56: 2919–30.

[41] Y. Wang, B. Gao, W. Woo, G.Y. Tian, X. Maldague, L. Zheng, Z. Guo, Y. Zhu. Thermal Pattern Contrast Diagnostic of Micro Cracks with Induction Thermography for Aircraft Braking Components[J]. IEEE Transactions on Industrial Informatics, 2018, 14: 5563 - 5574.

[42] J. Zhao, B. Gao, W.L. Woo, F.S. Qiu, G.Y. Tian. Crack Evaluation based on Novel Circle-ferrite Induction Thermography[J]. IEEE Sensors Journal, 2017, 17: 5637 – 5645.

[43] M.D. Iordache, J.M. Bioucas-Dias, A. Plaza. Collaborative Sparse Regression for Hyperspectral Unmixing.[J] IEEE Transactions on Geoscience and Remote Sensing, 2013, 52: 341–354.

[44] J.F. Cai, Cand, S Emmanuel J, Z. Shen. A Singular Value Thresholding Algorithm for Matrix Completion[J]. SIAM Journal on Optimization, 2008, 20: 1956–1982.

[45] J.M.P. Nascimento, J.M.B. Dias. Vertex component analysis: a fast algorithm to unmix

hyperspectral data[J]. IEEE Transactions on Geoscience and Remote Sensing, 2005, 43: 898–910.

[46] S.J. Wright, R.D. Nowak, M.A.T. Figueiredo. Sparse Reconstruction by Separable Approximation[J]. IEEE Transactions on Signal Processing, 2009, 57: 2479–2493.

[47] Zhou, Zihan, Xiaodong Li, John Wright, and Emmanuel Cand. Stable Principal Component Pursuit[C]. 2010 IEEE International Symposium on Information Theory.

[48] Feng, Jiashi. Xu, huan. Yan Shuicheng. Online Robust PCA via Stochastic Optimization[C]. In Advances in Neural Information Processing Systems 2013.